C.D. Slabaugh, I. Boxx, S. Werner, R.P. Lucht, W. Meier, Temporally-Resolved Measurements of the Structure and Dynamics in Partially-Premixed Swirl Flames at Elevated Power Density, AIAA J. 54, 946-961 (2016)

Original publication available at
http://arc.aiaa.org/doi/10.2514/1.J054294

Temporally-Resolved Measurements of the Structure and Dynamics in Partially-Premixed Swirl Flames at Elevated Power Density

Carson D. Slabaugh,* Isaac Boxx,† Stefanie Werner,‡ Robert P. Lucht,§ and Wolfgang Meier¶

The Turbomeca gas turbine model combustor was studied to understand the effect of increased thermal power density on the structure and dynamics of premixed swirl flames. The burner was operated under two flame conditions: one stable and one with self-excited thermo-acoustic oscillations. Simultaneous measurements of scalar and three-component velocity fields were acquired at $3\,kHz$ and $6\,kHz$ frequencies. Nonreacting flow measurements were used to approximate the spatial and temporal resolution with respect to the scales of the incoming flow. Time-resolved velocimetry revealed the presence of periodic fluctuations in both flames, occurring at shifted frequencies that did not correspond to a resonant acoustic mode or any corresponding harmonics. Proper Orthogonal Decomposition analysis revealed stably-forced inner shear-layer oscillations that periodically formed and ejected symmetric vortex pairs under stable flame operation. The unstable flame was found to exhibit a single spatio-temporally evolving flow structure consistent with a helical precessing vortex core. A reconstructed time series elucidated the interactions of the reactant jets, the precessing vortex core, and the central recirculation bubble over a thermo-acoustic cycle. This coupled interaction, and the resultant modulation of transport within the inner shear layer, were identified as a mechanism by which the precessing vortex core is linked to elevated power density flame dynamics.

Nomenclature

q	Chemical Heat Release $[a.u.]$
l_0	Integral Length Scale $[mm]$
t_0	Integral Time Scale $[ms]$
U	Flow Velocity $[m/s]$
ΔP	Injector Pressure Drop $[Pa]$
κ	Turbulence Spatial Scale in Wavenumber $[1/mm]$
ϕ	Fuel Equivalence Ratio
η_k	Kolmogorov Length Scale
Σ	Flame Surface Density $[1/mm]$
ω_z	Vorticity (z-rotation) $[1/s]$

Superscript

$'$	Fluctuation

Subscript

$_t$	Turbulence

Acronym

*Senior Research Engineer, Purdue University, Indiana, USA. Member AIAA.
†Research Associate, German Aerospace Center (DLR), Stuttgart, Germany. AIAA Associate Fellow.
‡Research Associate, German Aerospace Center (DLR), Stuttgart, Germany.
§Ralph and Bettye Bailey Professor of Combustion, Purdue University, Indiana, USA. AIAA Fellow.
¶Combustion Diagnostics Group Leader, German Aerospace Center (DLR), Stuttgart, Germany.

CRB	Central Recirculation Bubble
$FWHM$	Full-Width at Half-Maximum
$GTMC$	Gas Turbine Model Combustor
$HIPOT$	HIgh Pressure Optical Test rig
ISL	Inner Shear Layer
OSL	Outer Shear Layer
POD	Proper Orthogonal Decomposition
PVC	Precessing Vortex Core

I. Introduction

The principal challenge in the study of turbulent combustion is to sufficiently resolve the broad spectra of spatial and temporal scales over which the rate-controlling processes occur. As a nonergodic coupling of fluid mechanics and chemistry, turbulent flame behavior is governed by the interaction of these scales with nonlinear sensitivity to their local manifestation and relative strength. Turbulence controls the transport of heat and mass within the flow and, consequently, the structure of the flame. In turn, chemical reactions change the thermo-physical properties of the flow, which couple back to the fluid dynamics.[1–6] In modern propulsion and energy systems, the spectrum of scales over which these interactions take place is broadened by high turbulence Reynolds numbers, complex fuels, complex geometries, and many other factors. Now utilized as a design tool for such systems, large eddy simulation (LES) has evolved from the research domain into industrial sectors where these complex interactions are modeled (instead of resolved) to maintain affordable computational cost. Consequently, there is great need for high-bandwidth, high-resolution experimental measurements to support the development and validation of these computational combustion models at flow conditions that are representative of actual system operation.[7,8]

Swirling flows are known to contain highly-complex, unsteady features that can dominate the structure and dynamics of the velocity field.[9,10] Chemical reactions can alter spatial and temporal characteristics of these structures in complex ways as a function of the flame thermal power, local heat release field, swirl strength, and many other parameters. Consequently, the fundamental mechanisms of aerodynamic stabilization are highly dynamic and dependent on the instantaneous flow field. The simultaneous application of multi-kilohertz scalar and velocity field measurement techniques can provide time-resolved measurements of large-scale flow dynamics, yielding a greater understanding of flow-flame interactions by resolving the temporal evolution of transient phenomena such as thermo-acoustic oscillations.[11–17]

The objective of this work was to perform high-speed, simultaneous measurements of velocity and multiple scalar fields in a well-defined swirl combustor to study the effects of increased thermal power density on the structure and dynamics of the flow. As a target case for the International Workshop on Measurement and Computation of Turbulent Flames, the Turbomeca (Preccinsta, or TM-burner) gas turbine model com-

bustor (GTMC) has been the subject of extensive experimental and numerical investigation at atmospheric pressure.[18–25] In a distinct range of operation, this GTMC has been shown to exhibit strong self-excited thermo-acoustic pulsations. Meier et al.[18] performed a detailed experimental characterization of this unstable operation by studying two flame conditions: one *quiet* flame ($\phi = 0.83$, $P_{th} = 30\,kW$) and one with pronounced, self-excited, thermo-acoustic pulsations ($\phi = 0.70$, $P_{th} = 25\,kW$). Utilizing laser Doppler velocimetry (LDV), OH* chemiluminescence (OH*-CL), OH planar laser induced fluorescence (OH-PLIF), and laser Raman scattering, significant differences were observed between the quiet and the unstable flames with respect to the turbulent flow structure, mixing characteristics, flame shape, and the reaction progress. These results showed that the feedback loop for the sustained, self-excitation of thermo-acoustic oscillations in the Turbomeca GTMC (at atmospheric pressure) was an oscillation in mixture fraction coupled with a convective time delay. This conclusion was reinforced by the work of Franzelli et al.,[25] who performed LES computations to study the effects of incomplete mixing observed by Meier et al.[18] These computations confirmed that the pressure oscillations in the combustor caused a velocity fluctuation in the swirler, where fuel is introduced. This lead to a periodic accumulation and downstream convection of high equivalence ratio fuel-air mixture into the combustion chamber, evidently triggering the unsteady mode of heat release.

In the continued work of Meier et al.,[19] the time-evolution of cyclic variations in the flow and flame structures were captured over the course of the periodic cycle using simultaneous stereoscopic particle image velocimetry (SPIV) and OH-PLIF data acquired at $5\,kHz$. These measurements also revealed large-scale vortical structures that appeared near the nozzle exit and propagated downstream along the inner shear layer (ISL), which separates the central recirculation bubble (CRB) from the jet inflow. Boxx et al.[20] performed a proper orthogonal decomposition (POD) analysis to deconvolve these energetic structures and study their temporal content. A spatio-temporally evolving helical precessing vortex core (PVC) was isolated in the unsteady flame and was found to have a precession frequency of $570\,Hz$. The measured frequency of the thermo-acoustic oscillation was $288\,Hz$, very nearly the (1/2) subharmonic of the PVC precession frequency. Measurements in the quiet flame showed no clear evidence of a PVC, but did show a local periodicity in the ISL consistent with the periodic formation and ejection of symmetric vortex pairs. As a delineating factor between stable and unstable operation of the flame, it was concluded that a strong coupling existed between the heat release oscillations and the dynamics of the helical structure. Steinberg et al.[21] continued to investigate these affects with a parametric study of the dynamics of the PVC over a variety of nonreacting and combusting flow conditions, using high-speed SPIV and OH-PLIF. The flame was operated in a fully-premixed mode to alleviate the mixing dynamics reported by Meier et al[18] and Franzelli et al.[25] It was shown that the dominant flow structure, under nonreacting conditions, was again a helical precessing vortex core that rotated around the burner at a constant Strouhal number of 0.78 (where $St = \left(f_{PVC}\; d_{nozzle}\right) / u_{x,bulk}$).

Under reacting flow conditions, the characteristic frequency of the PVC was altered, but again, the precession was described by a constant Strouhal number of 0.88 in the cases where the PVC was detected, regardless of thermal power or equivalence ratio. As predicted by the simulations of Roux et al.,[22] and as previously observed by Boxx et al.,[20] in some cases the PVC was completely damped by combustion, particularly at low thermal power and high equivalence ratio conditions. In these cases, the most energetic flow structure dynamics were again observed to be periodic shear layer oscillations that shed vortices at the frequency of the thermoacoustic oscillation. Steinberg et al. concluded that there exists a distinct relationship between the pressure oscillation amplitude and the dominant structures present in the flow; specifically, that significantly greater pressure oscillation amplitudes are found in the cases presenting helical vortex cores than those with ejected vortices.

While the motivation to acquire high-bandwidth measurements in high-power-density flames is clear, there many putative challenges to be overcome. In the work of Boxx et al.,[26] simultaneous PIV/OH-PLIF and simultaneous PIV/OH* chemiluminescence measurements were acquired at a sustained 3 kHz repetition rate in a 120 kW flame operating at $0.5\,MPa$. This work established the feasibility of acquiring high-speed OH-PLIF measurements at these elevated conditions using the robust Diode-Pumped Solid-State (DPSS) laser platform, despite characteristically low laser pulse energy. The authors observed strong laser sheet absorption effects, which restricted the utility of the OH-PLIF data. However, it was shown that information about the large-scale dynamic behavior of the flow and flame could be extracted from the simultaneous complementary high-speed diagnostics. More recently, Slabaugh et al.[27] extended the application of DPSS-based laser systems to perform simultaneous $5\,kHz$ PIV/OH-PLIF measurements in a liquid-fueled, aeropropulsion combustor at up to $1.4\,MPa$ and $700\,kW$. In that study, the authors did not observe strong absorption effects, even at very high thermal loads. However, strong refractive index variation within the inner structure of the flame was found to cause defocusing of the PIV particle images and reduced spatial resolution (due to increased noise) in the computed vector fields. A baseline statistical analysis of the resolved scales was performed to further elucidate the flame characteristics that could extracted from the measurements.

In this work, simultaneous planar measurements of scalar and three-component velocity fields were acquired at $3\,kHz$ and $6\,kHz$ interrogation frequencies with OH-PLIF and stereoscopic PIV. The high-speed SPIV measurements are the first to be demonstrated in an elevated power density reacting flow, and are a critical step towards understanding the highly complex, three-dimensional behavior of swirling flows in modern combustion technologies. The measurement resolution is defined relative to the scales of the flow, followed by an analysis of the resolved scales to understand the physical mechanisms of the combustion dynamics. Comparisons are also drawn between the present study and the results from previous investigations

at atmospheric pressure.

II. Experiment Configuration

With an extensive experimental and numerical database in place for atmospheric pressure flame conditions, the focus of the present work is to characterize the Turbomeca GTMC at elevated thermal power density operation. The geometry of the mixer and nozzle have remained unchanged, with fuel and air being *technically premixed* (not perfectly premixed[18]) in the swirler section using 12 radial vanes and 12 corresponding $1\,mm$ fuel injection ports. The exit of the nozzle is $27.85\,mm$ in diameter, with a rounded, conical center-body aligned to the central axis.

A. Test Rig and Flames

To study the behavior of the Turbomeca GTMC at elevated conditions, the burner was installed into the High Pressure Optical (HIPOT) test rig, which is operated at DLR-Stuttgart. As shown in Figure 1, the HIPOT rig provides excellent optical access to the flame zone, supporting the application of simultaneous planar measurement techniques. The combustion chamber is $200\,mm$ in total length with an $85\,mm$ square cross-section. At the exit of the combustion chamber, a contraction with a $33\,mm$ diameter orifice exhausts into the quench zone where a water-cooled throttle is used to back-pressure the test section. A controlled and metered mass flow rate of clean, dry, preheated air is supplied to the plenum section, which serves as the inlet to the combustor.

Full optical access to the flame is provided through all four walls of the combustion chamber using a series of fused quartz windows. The unique design utilizes two inner windows which are installed with a small gap between the window surfaces to form a channel. Cooling air is forced through this channel to *back-side* cool the inner windows, eliminating the need for film cooling or dilution air injection into the flame zone. All other test rig hardware is water-cooled with mass flow-rate and inlet/exit temperature measurements to quantify heat loss to the combustor walls. The burner dome was designed with an impingement cooling circuit for high-power operation, but this feature was not found necessary in these tests. The dome temperature was measured to monitor rig health and to document flow boundary conditions.

The air mass flow rate to the experiment is set with a control valve and measured with a Coriolis flow meter while the fuel mass flow-rate is set using an electromechanical mass flow controller. All operating conditions, including pressures, temperatures, and air/fuel/water mass flow rates were monitored and recorded at a $1\,Hz$ interval. Dynamic pressures were also measured in the upstream plenum, the combustion chamber, and the downstream section with high-frequency piezo-resistive pressure transducers (Kistler 4043A with a 4603A amplifier). The signals were recorded, simultaneously (with dedicated A/D converters) at $100\,kHz$

along with the intensifier gate signal from the OH-PLIF detection system in order to synchronize the optical measurements to the measured acoustic signals.

[Figure 1 about here.]

Summarized in table 1, two flame conditions were chosen for this study: one stable (flame A) and one which exhibited self-excited thermo-acoustic oscillations (flame B). These flames were selected after extensive parametric variation of the inlet mass flow rate, pressure, and temperature as well as the equivalence ratio (ϕ); mapping the operability limits of the burner based on the flame structure and stability. The inlet air mass flow rate, pressure, and temperature are fixed, maintaining a constant bulk velocity of $55\,m/s$ and a Reynolds number, based on the non-reacting flow, of 1.3×10^5. Condition NR (Non-Reacting) was studied as the baseline flow while the two reacting flow conditions are distinguished simply by the fuel mass flow rate. Flame A was operated at an equivalence ratio of 0.70 while Flame B had an equivalence ratio of 0.58, resulting in thermal powers of $180\,kW$ and $150\,kW$, respectively. Though Flame B was found to have strong thermo-acoustic oscillations, it did not present any tendency toward complete blow-out at this condition. The experiment was always given a minimum of 10 minutes to stabilize, prior to acquiring measurements. At all conditions, $5\,g/s$ of unheated inlet air was diverted through the particle seeding system, then reintroduced to the inlet plenum. Though the particle seeding was limited to only short bursts during data acquisition, this unheated flow was maintained throughout the entire test by diverting it through a bypass circuit. This process ensured negligible impact on the combustor inlet conditions during data acquisition.

[Table 1 about here.]

B. Measurement Systems

In this work, simultaneous measurements of scalar and three-component velocity fields were acquired at a 3 kHz interrogation frequency using combined OH planar laser induced fluorescence (OH-PLIF), OH* chemiluminescence (OH*-CL), and stereoscopic particle image velocimetry (SPIV). Simultaneous SPIV and OH*-CL measurements were also acquired at 6 kHz for improved temporal resolution of flow-flame dynamics. A schematic representation of the optical measurement system configuration is given in Figure 2 with detailed descriptions of each individual sub-system provided below.

[Figure 2 about here.]

1. Stereoscopic Particle Image Velocimetry

A dual-cavity, diode-pumped, solid-state Nd:YAG laser (Edgewave IS611-DE) provided $532\,nm$ light at $2.6\,mJ/pulse$ with a repetition rate 3 kHz for the SPIV measurements. Using two cylindrical lenses

($f_{PIV,1} = -30\,mm$, $f_{PIV,2} = 250\,mm$) in a cylindrical telescope arrangement, the beam was expanded to approximately 30 mm in height. The collimated sheet was then focused to a thin waist outside of the combustor using a third cylindrical lens ($f_{PIV,3} = 700\,mm$). In previous campaigns using the same optical configuration, the sheet thickness was measured to be $\cong 700\,\mu m$ (FWHM) within the interrogation window. The inter-pulse separation time was $3\,\mu s$. A fluidized bed particle seeder was used to seed TiO_2 particles ($1\,\mu m$ nominal diameter) into the main air flow. The scattered light from the particle field was collected through $200\,mm$ focal length, f/4.0 objective lenses (Nikkor IF-ED Micro) and recorded with two high-speed, Complementary Metal-Oxide Semiconductor (CMOS) cameras (LaVision HSS8). The cameras had sufficient on-board memory to acquire 5400 double-frame image pairs per run. Ultra-steep, narrowband interference filters ($3\,nm$ FWHM centered on $532\,nm$) were used to isolate the scattered light signal in the highly luminous flame environments. For the field of view indicated in Figure 1, the spatial resolution of the raw scattering images was $53\,\mu m/pixel$.

Image calibrations, scaling, and particle cross-correlations were performed using the multi-pass adaptive window offset cross-correlation algorithm in the LaVision commercial software (DaVis 8.2.0). Results presented in this work were processed using a final window size of 24×24 pixels with 50 % overlap. The corresponding window resolution is $1.25\,mm$ with vector spacing of $0.63\,mm$. A local median filter, based on a 3×3 pixel square kernel, was used to remove spurious vectors beyond a specified threshold and find a replacement at a secondary (or tertiary) displacement correlation peak. With 5400 shots, each dataset was of sufficient length to achieve mean standard error (SE_m) convergence of $<1\,\%$, where $SE_m = \sigma/\sqrt{n}$ (σ is the standard deviation and n is the sample size).

2. Planar Laser Induced Fluorescence

The OH-PLIF laser system consisted of a frequency-doubled dye laser (Sirah Cobra-Stretch HRR) pumped by a Q-switched, diode-pumped, solid-state Nd:YLF pump laser (Edgewave IS811-E). Using Rhodamine 590 dye (in ethanol), the $566.4\,nm$ fundamental wavelength was frequency-doubled to $283.2\,nm$ to excite the $Q_1\,(7)$ line of the $A\ ^2\Sigma^+(v' = 1) \leftarrow X\ ^2\Pi(v'' = 0)$ transition of the hydroxyl radical. The average laser pulse energy at $283.2\,nm$ was $0.25\,mJ/pulse$ at a 3 kHz repetition rate. The PLIF excitation sheet was formed using two cylindrical lenses ($f_{PLIF,1} = -50mm$, $f_{PLIF,2} = 150mm$) in a cylindrical telescope arrangement, resulting in a collimated sheet height of approximately $20\,mm$. A third cylindrical lens ($f_{PLIF,3} = 750mm$) was used to focus the sheet to the beam waist ($\approx 400\mu m$ FWHM) at the combustor centerline.

The fluorescence signal was collected using a $64\,mm$ focal length, f/2.0 objective lens (Halle). A two-stage, lens-coupled intensifier (LaVision HS-IRO) was used to amplify the signal, which was imaged by a high-speed

CMOS camera (LaVision HSS6). The intensifier gate width was run at the minimum value possible (100 ns) to minimize background noise from flame luminosity. An optical band-pass filter isolated the fluorescence signal from the $A\ ^2\Sigma^+(v'=1) \rightarrow X\ ^2\Pi(v''=1)$ and $A\ ^2\Sigma^+(v'=0) \rightarrow X\ ^2\Pi(v''=0)$ bands occurring over the $305-315\,nm$ range of wavelengths.

3. Chemiluminescence

Chemiluminescence from electronically-excited hydroxyl (OH*) was imaged using a high-speed CMOS camera (LaVision HSS5) coupled to an external two-stage intensifier (LaVision HS-IRO). The line-of-sight integrated signal was collected using a $45\,mm$ focal length f/1.8 objective lens (Cerco Sodern Type-2073) while an interference filter isolated the OH*-CL signal over the $305-315\,nm$ range of wavelengths. An intensifier gate width of $25\,\mu s$ was used for all of the acquired datasets. The field of view for the OH*-CL system was approximately $65\times 80\,mm$ to capture the full spatial extent of the flame zone.

4. Simultaneous Integration

The laser sheets from the OH-PLIF system and the double-pulsed SPIV system were overlapped using a dichroic mirror, which had high transmissivity at 532 nm, and high reflectivity at 283 nm. Alignment and overlap of the lasers sheets was confirmed in the near and far-field. Image system calibrations were performed by imaging a dual-sided, dual-plane dot target (LaVision Type 07). The same target was used for the SPIV, OH-PLIF and OH*-CL systems, hence spatial alignment of all three measurement fields was achieved by mapping to the same coordinate system. Temporal synchronization of the lasers and imaging systems was accomplished with a digital delay pulse generator (Quantum Composers Model 9528). The 283 nm OH-PLIF laser pulse was delayed from the first 532 nm PIV pulse by $\Delta t/2$ (1.5 μs), while the OH*-CL IRO gate open time was delayed $5\,\mu s$ from the second PIV laser pulse. Timing was continuously monitored throughout the tests using an array of photodiodes and an oscilloscope.

III. Measurement Demonstrations

As this study represents the first simultaneous application of kHz acquisition-rate SPIV and OH-PLIF in a high pressure test rig, we begin by examining the quality of the measurements and quantifying the spatial and temporal resolution with respect to the scales of the flow.

A. Signal Quality

Figure 3 represents a typical instantaneous set of simultaneously-acquired measurements at flame B operation. An on-chip dark-field subtraction was performed prior to data acquisition. After the images were

corrected for distortion, cropped, and scaled to engineering units, a white-field normalization was also applied to the OH*-CL and OH-PLIF images to correct for pixel-to-pixel sensitivity variation in the HS-IRO/CMOS detection system.

[Figure 3 about here.]

As shown in Figure 3 (top), the OH*-CL signal was adequately strong with a $25\,\mu s$ gate width to effectively image the line-of-sight averaged structure of the flame and global heat release dynamics over a large field of view.[28,29] The simultaneously-acquired OH-PLIF image is shown in Figure 3 (bottom, left), where the direction of the laser sheet propagation is in the $(-)\,Y$ direction. The time-averaged peak OH-PLIF signal-to-noise ratio was approximately 16, where the detector noise was estimated using a series of homogeneous white-field images acquired at comparable levels of signal and gain. While the image does show some indication of laser-sheet absorption effects (evidenced by the signal attenuation in the direction of sheet propagation[30]), the overall quality of the OH-PLIF measurements was high enough to successfully apply the low SNR flame-front extraction methodologies described in Boxx et al.[26] and Slabaugh et al.[27] The resultant parametric contour function describing the *in-plane* flame surface topography ($f_i = x_{fi}\left(\xi_i\right)\hat{x} + y_{fi}\left(\xi_i\right)\hat{y}$) is shown as a thick black line overlaid against the OH-PLIF image. The quality of the SPIV particle images was quite good, and, consequently, the vector fields are as well. The single-shot, ensemble mean and fluctuation RMS of the normalized correlation strength were approximately 0.45 and 0.15, respectively, corresponding to a three-component velocity magnitude dynamic range of $10 - 120\,m/s$. Instantaneous vector fields were typically generated with $90 - 95\,\%$ first or second-choice correlation peaks while the number of filtered spurious vectors was consistently less then $5\,\%$ of the total vector count.

[Figure 4 about here.]

Figure 4 shows a sequence of measurements acquired at the $3\,kHz$ interrogation frequency in the unstable flame (flame B). At $3\,kHz$, the evolution of the limit-cycle thermo-acoustic behavior is captured over six measurements, where strong fluctuations in the global heat release can be observed from the OH*-CL time series. The SPIV velocity measurements also show strong fluctuations in both the reactant jet flow and the structure of the central recirculation, as well as the width of the shear layer separating these two dominant flow features. The detected flame surface contours show good correspondence with the measured flow structure, with the reaction zones remaining roughly aligned with the inner shear layer between the reactant jet and the central recirculation bubble and located at a slightly shifted position into the jet. The planar flame topography is also in visual agreement with the spatio-temporal evolution of the OH*-CL images. As shown, this correspondence is suitably robust throughout the cycle, despite extremely large variation in heat release (signal) levels. Hence, this figure illustrates the capacity of the high-speed measurement system

to instantaneously resolve the large scale flow-flame dynamics occurring at the thermo-acoustic frequency. It provides a testament to the suitability of the spatial and temporal dynamic range of the measurement systems and data extraction procedures for continued analysis of the targeted flame physics.

B. Resolution Considerations

In turbulent combustion, the distribution of turbulence energy over the spatial and temporal scales present in the flow is a critical element of flame behavior. Preceding the detailed extraction and analysis of flow physics from a velocimetry dataset, it is therefore crucial to establish the measurement bandwidth relative to the turbulence energy spectrum. In this section, the integral time scales and integral length scales are computed and utilized as a basis to establish the true resolution with respect to the most energetic scales of the flow.

To begin, the temporal autocorrelation was computed from a time series of axial velocity extracted at three points in the flow corresponding to the known dominant structures: the reactant inflow jet (P1), the central recirculation bubble (P3), and the inner shear layer (P2) separating the jet and the central recirculation bubble (see Figure 11 for reference in flames A and B). The correlations were computed with an FFT-based method using a convolved Hann windowing function, then rescaled to recover the original variance. As shown in Figure 5, within the jet (P1) the temporal correlation decays quite rapidly, with $Q_{ij}(\Delta t) \rightarrow 0$ around $\Delta t \approx 0.5\,ms$. The integral time scale (t_0) was computed as $\int_0^{\Delta t_0} Q_{ij}(\Delta t) d\,(\Delta t)$, where $\Delta t_0 = \Delta t\,|_{Q_{ij}=0}$ and found to be $44.2 \mu s$ in the nonreacting jet. Assuming an integral length scale (l_0) of approximately one-half the burner annulus height ($\approx 5\,mm$) and assuming a $110\,m/s$ mean jet velocity, a first-order estimation of t_0 is $45.4\,\mu s$, so this result is quite feasible. Thus, at a sampling rate of $166.7\,\mu s$, it is clear that the temporal evolution of the jet hydrodynamics will not be resolved. At both P2 and P3, however, a consistent periodic oscillation remains after the initial correlation decay. With an amplitude of $Q_{ij} \approx 0.2$ and a period of $\sim 550\,\mu s$, it will later be shown that this fluctuation corresponds to the spatio-temporal evolution of a helical precessing vortex core (PVC) which has a characteristic frequency of $1800\,Hz$ at condition NR. Evidently, at a $6\,kHz$ interrogation frequency, these measurements are sufficient to resolve the large-scale, coherent, energetic flow features in the ISL and CRB regions of the inlet flow to the high-power flame.

[Figure 5 about here.]

Discrete spatial correlations were computed to extract the value of the integral length scales in this windowed region of the flow. It should be noted that spectral analysis of spatial coherence in the flow carries the implicit assumption that the turbulence field is statistically homogeneous in nature.[3,31] Again, utilizing the nonreacting velocity field data from condition NR, the fluctuating velocity field was sampled from a

windowed region within the boundaries of the in-flowing jets (shown previously to adequately resolved in time). The ensemble averaged lateral and longitudinal two-point correlations are given in Figure 6.

[Figure 6 about here.]

One possible explanation for dissimilarity between Q_{11} and Q_{22} in both the lateral and longitudinal correlations is simply that the flow is not statistically isotropic, which is very reasonable to expect, given flow complexities that are concomitant with high-power gas turbine combustors. An additional explanation stems from the presence of optical astigmatism on the SPIV particle image fields; found to be a consequence of the oblique viewing angle through the series of test rig windows. As it is shown in Figure 7, the sub-pixel sized particles are imaged in sharp focus in the X direction, but in the Y direction they are blurred over $\sim 4 - 8\, pixels$. As a result, there is a similar smoothing of the displacement correlation peak (also shown in Figure 7). The accuracy of PIV displacement evaluation algorithms is a function of the uncertainty in the location of the particle image centroid and the correlation peak centroid. Sub-pixel resolution of the computed displacement is obtained from the *gray* values around the intensity normalized displacement correlation peak using three-point estimators of peak centroid. Broadening of the correlation peak will increase the random noise in the computed velocity field and, in particular, in the fine scales of the flow which are more sensitive to the accuracy of sub-pixel displacement computations.[32, 33]

[Figure 7 about here.]

These effects are seen in the computed one-dimensional turbulent kinetic energy spectrum, where, at high wavenumber, there is a non-physical increase in the measured turbulent kinetic energy. This *tail* is a result of an accumulation of noise from the cross-correlation algorithm as well as other spatial aliasing effects; evidence of the well-known trade-offs in PIV measurements between signal, resolution, and the system dynamic range.

[Figure 8 about here.]

It is concluded that the true spatial resolution of the SPIV measurements is not determined solely by the detector hardware, but is also a function of the data processing algorithms and even the flow itself. Hence, the spatial resolution cut-off for the present SPIV measurements is approximated to be $900\,\mu m$, based on the location of the *roll-up* of the ensemble-averaged turbulent kinetic energy spectrum shown in figure 8. The integral length scale (l_0), computed as $\int_0^{r_0} Q_{11}(\vec{r})d\vec{r}$, where $r_0 = \vec{r}|_{Q_{11}=0}$ was found to be $2.7\, mm$ and $4.4\, mm$ based on the lateral and longitudinal correlation of the axial velocity component (Q_{11}), respectively. Again, with an annulus height of approximately $10\, mm$ and an inlet jet axial velocity full-width at half-max of $\sim 8\, mm$, the calculation is quite reasonable. Hence, the SPIV spatial resolution, defined relative to the integral length scale of the nonreacting turbulent flow, is estimated to be $l_0/4$.

IV. Results and Discussion

A. Time-Averaged Statistics

Figure 9 provides a comparison of the time-averaged OH*-CL, OH-PLIF, and SPIV measurements. As expected, the principal flow features are clearly resolved: a high-velocity inflow (the reactant *jet*), a large central recirculation (the central recirculation bubble, or *CRB*), and shear layer at their interface (the *ISL*). The flame is considerably more compact under operation at elevated pressure and temperature, as one might expect based on the increased inlet temperature, pressure, and turbulence Reynolds number (Re_t).[18,20]

[Figure 9 about here.]

Several distinctions between flames A and B are evident in the measured data. Consistent with measurements at atmospheric pressure, the stable flame condition (A) has a wider jet-opening angle than the unstable case. The reactant jets of flame A also maintain a more narrow high velocity core accompanied by a more gradual velocity decay along the jet trajectory. In contrast, the time-averaged velocity field in flame B shows a more rapid breakdown of the jet, indicated by a broadened jet width as well as a broadened inner-shear layer. The reversed flow velocity magnitude in the CRB is also notably greater in flame B, than in the stable flame A.

The time-averaged OH*-CL emission from flame A is significantly more intense than what is measured in flame B (note the difference in color scale), where the peak axial and radial extent of the OH* emission is broadened by the flame dynamics. A planar representation of the flame surface density (Σ) was computed by summing the occurrences of the flame surface contour function (described in Section IIIA) within $1\,mm$ square windows, then ensemble-averaging in time. As a planar slice of the line-of-sight averaged OH*-CL field, Figure 9(c) captures the same trend as this cross-sectional cut through the flame centerline.

B. Temporal Content

Figure 10 shows the power spectra of the global flow and flame measurements performed. The dynamic combustion chamber pressure (p') was measured on the burner dome. The global chemiluminescence intensity (q') is the fluctuation of the integrated pixel intensity value conditioned on threshold minimum; $q = \sum_{x,y=0}^{max} I(x,y)|_{I>I_o}$, where I_0 is a scalar threshold slightly greater than the sensor noise level. The chamber volume influx fluctuation (v') is from computed by integration of the axial velocity component over the entire channel width at a fixed axial position at $x = 6\,mm$.

[Figure 10 about here.]

The power spectra chamber pressure and integrated OH*-CL emission for flame A show strong peaks at $480\,Hz$ indicating, that although the flame was stable, it exhibited a periodic oscillation at a characteristic

frequency. Flame B also has a distinct peak in the p' power spectrum at $450\,Hz$. Scaling with the acoustic speed, this characteristic frequency is likely a resonant acoustic mode of the system, though the exact nature of this resonance is not immediately apparent from these measurements. Nonetheless, the low peak amplitudes of the p' and q' power spectra in flame A, compared to flame B, suggest that this mode is heavily damped. Also, the absence of a corresponding peak in the v' signal of flame A indicates negligible coupling between the combustion chamber oscillations and the reactant supply system. In contrast, flame B shows distinct and powerful peaks at $450\,Hz$ in all three signals, corresponding to the dominant frequency of the thermo-acoustic oscillation.

[Figure 11 about here.]

To better understand the physical processes controlling this instability, an axial velocity time series was again sampled from the *time-resolved* SPIV measurements at three locations within the dominant flow structures (shown in Figure 11). As anticipated, based on the velocity autocorrelation and integrated signals analysis, the jet time series did not show any strong spectral content at the resonant frequency in flame A, while flame B exhibited a single, distinct peak at $450\,Hz$ that was caused by the coupling of the thermo-acoustic pulsation to the reactant supply. In flame A, the ISL and CRB both show very weak spectral content at $480\,Hz$, which is reasonable to expect, considering that there was an observed (albeit weak) frequency response in the flame heat release rate, q'. Also present is a band of more powerful frequency content centered around $1830\,Hz$. Similarly in flame B, the ISL and CRB probes shared not only a strong, distinct peak at $450\,Hz$, but also presented another broad frequency band centered at $1710\,Hz$.

[Figure 12 about here.]

The spectral content of the ISL and CRB have revealed distinct periodic phenomena occurring locally within the flow-field in regions that can be well-resolved (in space and time) by the current measurement set. The absence of corresponding $1830\,Hz$ and $1710\,Hz$ peaks (or their harmonics) in the p', q', and v' spectra suggests that these physical processes may not be strongly coupled. However, given the wide range of complex flow processes that can affect these structures, the nature and corresponding influence of these fluctuations is not immediately clear.

C. Proper Orthogonal Decomposition

To further characterize the velocity fluctuations observed in the time-resolved, SPIV data probes, a spatio-temporal proper orthogonal decomposition (POD) was performed. POD is a well-established technique used to identify the most energetic features of the velocity field in a mathematically-rigorous manner.[34–36] The POD analysis of n measurement realizations will yield a set of n spatial eigenmodes ($M_j\,(x, y)$) with

corresponding temporal coefficients ($a_j(t)$) and eigenvalues (λ_j). The eigenmodes form an orthogonal basis of the original dataset and the eigenvalues provide a measure of the eigenmodes contribution to the total measured kinetic energy. Sorting the modes in descending order by the eigenvalue magnitude, the sum of the highest m eigenvalues will have greater total kinetic energy in the POD basis than any other orthogonal basis. Hence, the POD analysis can be (carefully) applied to study the most energetic structures of the flow in a deconvolved state. POD can also be utilized as a robust filter by reconstructing the dataset with only the most energetic features of the flow, which are represented by the first m most dominant modes, where $u_m(x,y,t) = \sum_{j=0}^{m} a_j(t) M_j(x,y)$. The POD analysis presented here was performed with 5400 SPIV vector fields measured at a 6 kHz interrogation frequency.

The zeroth eigenmode is the mean velocity field. Spectral analysis of $a_0(t)$ at the flame B condition shows a single peak at the thermoacoustic frequency, corresponding to the periodically fluctuating volumetric influx to the combustion chamber. Figure 13 shows the time history of the zeroth mode along with the q' and p' signals. There is clear coherence in the coupling of these signals, with the phase of the heat release oscillations only slightly lagging the pressure oscillations to drive the thermo-acoustic oscillation. Also, $a_0(t)$ (or similarly, v') and q' are almost completely out of phase, consistent with previous experimental and numerical works.[18,25]

[Figure 13 about here.]

The three most energetic fluctuation eigenmodes for each condition are shown in Figure 14. The eigenmodes are represented by the in-plane velocity vector field plotted over the out of plane vorticity (ω_z). The first two eigenmodes of flame A are symmetric and resemble a pair of jets with adjacent standing vortices centered at approximately $(12, \pm 16)\, mm$ and $(24, \pm 24)\, mm$ in modes 1 and 2, respectively. Spectral analysis of the temporal coefficients shows a similar broadband content again centered at approximately $1830\, Hz$. This is consistent with the frequency content identified in the velocity probes in the ISL and CRB. Taken as a pair, these two eigenmodes represent a stably forced shear layer with vortices being generated in the ISL at the $1830\, Hz$ characteristic frequency, then convected downstream along the trajectory of the ISL. Figure 15(a) shows the normalized temporal coefficient magnitude as a function of time. Modes 1 and 2 are have very similar profiles, but with a_2 leading a_1 by approximately one time-step ($167\, \mu s$). The displacement of the vortex pair between eigenmodes 1 and 2 occurring over a $167\, \mu s$ corresponds to an $87\, m/s$ velocity, which reinforces the interpretation of a convected vortex. The third eigenmode extracted from the flame A dataset is a symmetric pair of counter-rotating vortices. The associated temporal coefficient $a_3(t)$ showed strong periodic content at $480\, Hz$, though this frequency was not observed as a distinct peak in the velocity probe data. Thus, mode 3 is unlikely to have any strong physical significance with respect to the flow dynamics and is most likely counteracted by the sum of other higher modes. The POD analysis has elucidated that

the jet is the dominant flow structure in flame A. In the absence of a thermo-acoustically coupled instability, the energetic flow structures are simply the result of hydrodynamic instabilities and are not observed to have a significant impact on flame dynamics.

[Figure 14 about here.]

Modes 1-3 of the flame B case indicate a series of large scale vortices aligned with the trajectory of the ISL. A similar, weaker chain of vortices is also observed along the OSL, particularly in mode 3, but also in modes 1 and 2 to a lesser extent. Modes 1 and 2 are largely asymmetric, with shifted pairs of vortices having opposite rotation split across the flow centerline. In apparent counter-distinction, mode 3 exhibits nearly perfect symmetry in, what appear to be, two co-rotating vortex pairs. Closer examination, however, reveals that these are actually staggered, counter-rotating vortices, which are correlated with the identified vortices in modes 1 and 2. Spectral analysis of a_1, a_2, and a_3 shows nearly identical, bimodal frequency content; with one powerful, distinct peak at the frequency of the thermo-acoustic oscillation and a second, broad band of frequency content centered around $1710\,Hz$. As shown in Figure 15(b), all three of the temporal coefficients have very similar profiles, with each being phase shifted from the other by approximately 1/3 of the cycle period. The structural similarity of the first three eigenmodes coupled with the coherence of the associated temporal coefficients strongly suggests that these three modes correspond to a single spatio-temporally evolving coherent turbulent structure in the flow. Previous research on this burner geometry, at atmospheric conditions, suggests that this structure is a helical precessing vortex.[20,21]

[Figure 15 about here.]

D. Precessing Vortex Core

POD analysis revealed the presence of a helical vortex core in flame B; a large-scale turbulent structure that circumscribes the centerline of the combustor while expanding radially, with increasing axial distance, along the trajectory of the inner shear layer.[9,10,16] The strength of the eigenvalues indicates that the PVC is the dominant dynamic flow structure in flame B, with $> 70\,\%$ of the measured turbulent kinetic energy contained in the first three POD modes. The precession of the PVC occurs at approximately $1710\,Hz$ based on the strongest peaks in the power spectra of the temporal coefficients, aside from the narrow-band content at the thermo-acoustic frequency. Known to scale linearly with the bulk velocity,[10] Figure 16 shows the precession frequencies of conditions B and NR plotted against data from previous studies performed in the same combustor, at atmospheric pressure.[21] The agreement is quite strong in the reacting flow case, which was previously reported to maintain a constant Strouhal number 0.88 over all conditions in which the PVC was present, regardless of flame thermal power or equivalence ratio. Defined as $St = \left(f_{PVC}\; d_{nozzle}\right)/u_{x,bulk}$,

the Strouhal number of the PVC in flame B was calculated to be 0.87. The observed departure in the nonreacting case may be the result of a system acoustic mode, which would have significant impact on the dampening characteristics of hydrodynamic instabilities, particularly in the absence of combustion.

[Figure 16 about here.]

As previously observed under atmospheric pressure conditions,[19–22] this analysis has shown the PVC to be a delineating factor between stable and unstable flame behavior at elevated thermal power density. The second, $450\,Hz$ spectral peak, shared by POD modes 1-3, also suggests that the spatio-temporal dynamics of the PVC are coupled with the thermo-acoustic pulsation. However, with no measured spectral content in q', v', or p' in the range of $1710\,Hz$ (or any integer multiple thereof), the exact role of the PVC in the local coupling of flame dynamics remains unclear. Hence, it is of principal interest to determine how this hydrodynamic instability, with much shorter time-scales at elevated power density, couples to the resonant acoustic modes of the combustor and if these mechanisms are comparable to those previously elucidated in less energetic, laboratory-scale flows.

E. Central Recirculation Bubble Dynamics

In swirl combustors, the CRB plays a critical role in the stabilization of the flame by transporting heat and radicals from the combustion products back upstream to the flame root; sustaining ignition and controlling fluid residence times. The recirculation of high-temperature, high-viscosity gases within the CRB can drastically alter the structure and strength of the PVC and, in cases such as flame A, can even dampen it completely. On the other hand, the PVC can affect the shape of the CRB and the mixing characteristics within the ISL. Hence, the susceptibility and relevance of PVC-CRB dynamics to thermo-acoustic instabilities in high-power flames is of principal interest.

Figures 17 and 18 present a time sequence of the flame B velocity field over one thermo-acoustic cycle, to draw a phenomenological understanding of the spatio-temporal evolution of these unsteady combustion processes. These velocity fields represent the most energetic structures of the flow; reconstructed from the first ten modes of the POD to recover $> 90\,\%$ of the original, measured turbulent kinetic energy. The CRB is visualized in Figure 17 by an isocontour of $U_x = 0$, defining the stagnation line of the ISL and the boundary of the CRB. Overlaid against contours of out-of-plane vorticity (ω_z) to visualize the PVC, the temporal evolution of coupled interactions between these two flow structures can be studied. Figure 18 provides an understanding of the local velocity field contained within these features, overlaid against contours of axial velocity to distinguish the inflow jets, the CRB, and the ISL. Figure 19 presents the pressure difference across the swirler ($p'_p - p'_c$) with the data points corresponding to the time at which each instantaneous velocity field was acquired. The time axis has been shifted to correspond with the time-stamp labels in the

sequence figures (17 and 18). The normalized fluctuation amplitudes of the upstream plenum pressure (p'_p), the combustion chamber pressure (p'_c), and the flame heat release (q') are also included in Figure 19 for reference.

[Figure 17 about here.]

[Figure 18 about here.]

[Figure 19 about here.]

To begin, the first four images represent approximately one single precession of the PVC, which has a period of approximately $580\mu s$. This is clearly shown, in Figure 17, by the axially-staggered (across the flow centerline) pockets of vorticity along the ISL. The local rotation of the PVC is correlated with wrinkling of the stagnation lines, which increases the surface area over which the jets and the CRB interact. Recalling that reaction front tends to align with the stagnation line along the ISL (Figure 4), it is understood that strong dynamics in the structure and spatial location of the stagnation line will be coupled with dynamics in the reaction zone. As the azimuthal precession progresses, the corrugated regions of the stagnation lines are swept downstream, while they remain enmeshed with the spatio-temporal evolution of the PVC. The axially-staggered, conjugate nature of these corrugations, across the flow centerline, suggests that the stagnation surface (the outer boundary of the CRB) is also helical in nature, as it has been shaped by the PVC.[9,10]

As shown in Figure 19, the peak in heat release occurs at approximately $t = 0.167\,ms$. Immediately thereafter, the axial velocity magnitude of the inflow jets begins to increase (Figure 18) as the chamber pressure drops and the pressure difference across the swirler climbs. Starting at $t \approx 0.667\,ms$, the CRB begins to swell in response to the growing strength of the swirling inflow. Figure 18 shows a corresponding surge of $-U_x$ back into the CRB that continues until approximately $1.333\,ms$. The swell of the CRB is shown to cause significant compression of the ISL in Figure 18 accompanied by axial stretching of the PVC aligned along the stagnation line, as seen clearly in Figure 17. Evidently, as the PVC cross-section is stretched in-plane, ω_z, S_{ij}, and, consequently, transport within the ISL will be significantly impacted. Figure 18 also shows swelling of the CRB impacts inflow jets as they are forced radially outward from $t = 0.833\,ms \rightarrow t = 1.167\,ms$, at the peak of the ΔP fluctuation. The PVC is reestablished at $t \approx 1.5\,ms$, and the coupled PVC-CRB dynamics return to a $1710\,Hz$ periodic azimuthal precession. As time proceeds ($t > 1.667\,ms$), the chamber pressure again climbs and the correspondingly injector pressure drop falls. The following peak in p' and q' ($t \approx 2.333\,ms$) indicate the start of the next thermo-acoustic cycle.

As previously discussed, the bimodal behavior of the POD temporal coefficients corresponding to the first three POD modes of flame B ($a_1(t)$, $a_2(t)$, and $a_3(t)$ in figures 14 and 15(b)), indicate two characteristic frequencies in the PVC dynamics: 1) the precession frequency, at $1710\,Hz$ and 2) the thermo-acoustic

frequency, at $450\,Hz$. It was anticipated that the latter would correspond to local flow-flame interactions in the ISL. Instead, it was found that there exists is a remarkable similarity in the structure of the flow measured from $t = 1.667 \rightarrow 2.333\,ms$ and $t = 0 \rightarrow 0.667\,ms$; times which correspond to rapid, high-amplitude fluctuations in both chamber pressure (p') and flame heat release (q') (Figure 19). Consistent throughout the measurement series, the temporal evolution of this process can be seen in the simultaneous amplitude modulation of the normalized temporal coefficients of modes 1-3 (Figure 15(b)). This suggests that the structure of the PVC is, instead, more strongly correlated to the local dynamics of the central recirculation bubble. Particularly, it is the swell and deflation of the CRB, and its corresponding modification of the PVC, that is captured by the $450\,Hz$ spectral peaks in $a_1(t)$, $a_2(t)$, and $a_3(t)$. This coupled interaction, and the resultant modulation of mixing characteristics in the ISL, is identified as a potential mechanism by which the PVC could be linked to elevated power density flame dynamics, despite having largely varying (inharmonic) time-scales.

V. Conclusion

In summary, this study demonstrated simultaneous multi-scalar and three-component velocity measurements acquired at multi-kHz interrogation frequencies in two lean, technically-premixed swirl flames operating at elevated pressure and thermal power. Flame A was stable, while flame B exhibited strong, self-excited thermoacoustic pulsations. Baseline measurements in the corresponding, nonreacting flow were used to estimate the true measurement resolution with respect to the spatial and temporal scales of the incoming flow. At $6\,kHz$, the temporal resolution of the measurements was sufficient to capture the large-scale flow and flame dynamics within the inner shear layer and central recirculation bubble. The spatial resolution of the SPIV measurements in these regions was approximately $l_0/4$. An analysis of the time-averaged flow and flame structure revealed significant variance between the stable and unstable operating conditions. Further investigation of the time-resolved velocimetry revealed the presence of periodic velocity fluctuations in both flames, but at shifted frequencies that did not correspond to a change in the acoustic speed or any of the corresponding harmonics. POD analysis of the velocity fields revealed stably-forced inner shear layer oscillations that periodically formed and ejected vortices under stable flame operation. The unstable flame, however, exhibited a single, dominant, spatio-temporally evolving flow structure. Identified as a precessing vortex core, the Strouhal number was 0.87, which was in good agreement with earlier studies performed in the same burner. A reconstructed time series from the $0^{th} - 10^{th}$ modes of the POD analysis was used to study the interactions of the reactant jets, the precessing vortex core, and the central recirculation bubble over a thermo-acoustic cycle. Consistent with prior studies of flames generated with this burner geometry, it was found that the structure of the PVC was strongly correlated with the local dynamics of the central

recirculation bubble. This coupled interaction, and the resultant modulation of mixing characteristics in the ISL, were identifed as a potential mechanism by which the PVC is linked to elevated power density flame dynamics. The fact that such interactions persist at conditions of high Re_t, pressure, and thermal load is an exciting new development in our understanding of this well-characterized burner configuration.

Acknowledgments

Carson D. Slabaugh acknowledges travel support from the John Zink Institute Fellowship Fund.

References

[1]Peters, N., *Turbulent Combustion*, Cambridge Monographs on Mechanics, Cambridge University Press, 2000.

[2]Poinsot, T. and Veynante, D., *Theoretical and Numerical Combustion*, CERFACS, 3rd ed., 2005.

[3]Pope, S. B., *Turbulent Flows*, Cambridge University Press, 2000.

[4]Bray, K., "The challenge of turbulent combustion," *Proceedings of the Combustion Institute*, Vol. 26, No. 1, 1996, pp. 1–26.

[5]Bilger, R., S.B., P., Bray, K., and J.F., D., "Paradigms in turbulent combustion research," *Proceedings of the Combustion Institute*, Vol. 30, 2005, pp. 21–42.

[6]Barlow, R., "Laser diagnostics and their interplay with computations to understand turbulent combustion," *Proceedings of the Combustion Institute*, Vol. 31, 2007, pp. 49–75.

[7]Selle, L., Lartigue, G., Poinsot, T., Koch, R., Schildmacher, K. U., Krebs, W., Prade, B., Kaufmann, P., and Veynante, D., "Compressible large eddy simulation of turbulent combustion in complex geometry on unstructured meshes," *Combustion and Flame*, Vol. 137, No. 4, 2004, pp. 489–505.

[8]Gicquel, L., Staffelbach, G., and Poinsot, T., "Large Eddy Simulations of gaseous flames in gas turbine combustion chambers," *Progress in Energy and Combustion Science*, Vol. 38, No. 6, 2012, pp. 782–817.

[9]Lucca-Negro, O. and O'Doherty, T., "Vortex breakdown: A review," *Progress in Energy and Combustion Science*, Vol. 27, 2001, pp. 431–481.

[10]Syred, N., "A review of oscillation mechanisms and the role of the precessing vortex core (PVC) in swirl combustion systems," *Progress in Energy and Combustion Science*, Vol. 32, No. 2, 2006, pp. 93–161.

[11]Carter, C. D., Donbar, J. M., and Driscoll, J. F., "Rapid communication Simultaneous CH planar laser-induced fluorescence and particle imaging velocimetry in turbulent nonpremixed flames," *Applied Physics B Lasers and Optics*, Vol. 66, 1998, pp. 129–132.

[12]Sadanandan, R., Stohr, M., and Meier, W., "Simultaneous OH-PLIF and PIV measurements in a gas turbine combustor," *Applied Physics B: Optics and Lasers*, Vol. 90, 2008, pp. 609–618.

[13]Stohr, M., Sadanandan, R., and Meier, W., "Experimental study of unsteady flame structures of an oscillating swirl flame in a gas turbine model combustor," *Proceedings of the Combustion Institute*, Vol. 32, No. 2, 2009, pp. 2925–2932.

[14]Bohm, B., Kittler, C., Nauert, A., and Driezler, A., "Diagnostics at high repitition rates: new insights into transient combustion phenomena," *Proceedings of the European Combustion Meeting*, 2007.

[15]Boxx, I., Stohr, M., Carter, C., and Meier, W., "Sustained multi-kHz flamefront and 3-component velocity-field mea-

surements for the study of turbulent flames," *Applied Physics B: Laser and Optics, Rapid Communication*, Vol. 95, 2009, pp. 23–29.

[16]Stohr, M., Boxx, I., Carter, C. D., and Meier, W., "Experimental study of vortex-flame interaction in a gas turbine model combustor," *Combustion and Flame*, Vol. 159, No. 8, 2012, pp. 2636–2649.

[17]Carter, C. D., Hammack, S., and Lee, T., "High-speed planar laser-induced fluorescence of the CH radical using the C2Sigma - X2Pi band," *Applied Physics B Lasers and Optics*, Vol. 116, 2014, pp. 515–519.

[18]Meier, W., Weigand, P., Duan, X., and Giezendannerthoben, R., "Detailed characterization of the dynamics of thermoacoustic pulsations in a lean premixed swirl flame," *Combustion and Flame*, Vol. 150, No. 1-2, 2007, pp. 2–26.

[19]Meier, W., Boxx, I., Stohr, M., and Carter, C. D., "Laser-based investigations in gas turbine model combustors," *Experiments in Fluids*, Vol. 49, 2010, pp. 865–882.

[20]Boxx, I., Arndt, C. M., Carter, C. D., and Meier, W., "High-speed laser diagnostics for the study of flame dynamics in a lean premixed gas turbine model combustor," *Experiments in Fluids*, Vol. 52, No. 3, 2010, pp. 555–567.

[21]Steinberg, A., Arndt, C. M., and Meier, W., "Parametric study of vortex structures and their dynamics in swirl-stabilized combustion," *Proceedings of the Combustion Institute*, Vol. 34, No. 2, 2013, pp. 3117–3125.

[22]Roux, S., Lartigue, G., Poinsot, T., Meier, U., and Berat, C., "Studies of mean and unsteady flow in a swirled combustor using experiments, acoustic analysis, and large eddy simulations," *Combustion and Flame*, Vol. 141, No. 1-2, 2005, pp. 40–54.

[23]Galpin, J., Naudin, A., Vervisch, L., Angelberger, C., Colin, O., and Domingo, P., "Large-eddy simulation of a fuel-lean premixed turbulent swirl-burner," *Combustion and Flame*, Vol. 155, No. 1-2, 2008, pp. 247–266.

[24]Fiorina, B., Vicquelin, R., Auzillon, P., Darabiha, N., Gicquel, O., and Veynante, D., "A filtered tabulated chemistry model for LES of premixed combustion," *Combustion and Flame*, Vol. 157, No. 3, 2010, pp. 465–475.

[25]Franzelli, B., Riber, E., Gicquel, L. Y., and Poinsot, T., "Large Eddy Simulation of combustion instabilities in a lean partially premixed swirled flame," *Combustion and Flame*, Vol. 159, No. 2, 2012, pp. 621–637.

[26]Boxx, I., Slabaugh, C. D., Kutne, P., Lucht, R. P., and Meier, W., "3 kHz PIV / OH-PLIF measurements in a gas turbine combustor at elevated pressure," *Proceedings of the Combustion Institute*, 2014, doi: 10.1016/j.proci.2014.06.090.

[27]Slabaugh, C. D., Pratt, A. C., and Lucht, R. P., "Simultaneous 5 kHz OH-PLIF/PIV for the study of turbulent combustion at engine conditions," *Applied Physics B: Lasers and Optics*, 2014, doi: 10.1007/s00340-014-5960-5.

[28]Lee, S., Seo, S., Broda, J., Pal, S., and Santoro, R., "An experimental estimation of mean reaction rate and flame structure during combustion instability in a lean premixed gas turbine combustor," *Proceedings of the Combustion Institute*, Vol. 28, No. 1, 2000, pp. 775–782.

[29]Hardalupas, Y. and Orain, M., "Local measurements of the time-dependent heat release rate and equivalence ratio using chemiluminescent emission from a flame," *Combustion and Flame*, Vol. 139, No. 3, 2004, pp. 188–207.

[30]Sadanandan, R., Meier, W., and Heinze, J., "Experimental study of signal trapping of OH laser induced fluorescence and chemiluminescence in flames," *Applied Physics B: Lasers and Optics*, Vol. 106, 2012, pp. 717–724.

[31]Monin, A., Yaglom, A., and Lumley, J., *Statistical Fluid Mechanics: Mechanics of Turbulence*, No. v. 1 in Dover books on physics, Dover Publications, 2007.

[32]Adrian, R. and Westerweel, J., *Particle Image Velocimetry*, Cambridge Aerospace Series, Cambridge University Press, 2010.

[33]Westerweel, J., *Digital Particle Image Velocimetry: Theory and Application*, Delft University Press, 1993.

[34]Berkooz, G., Holmes, P., and Lumley, J. L., "The proper orthogonal decomposition in the analysis of turbulent flows," *Annual Review of Fluid Mechanics*, Vol. 25, 1993, pp. 539–575.

[35]Sirovich, L., "Turbulence and the dynamics of coherent structures. Part I. Coherent structures," *Quarterly of Applied Mathematics*, Vol. 5, 1987, pp. 561–590.

[36]Roy, S., Hua, J. C., Barnhill, W., Gunaratne, G. H., and Gord, J. R., "Deconvolution of Reacting-Flow Dynamics Using Proper Orthogonal and Dynamic Mode Decompositions," *Physical Review E*, Vol. 91, 2015.

List of Figures

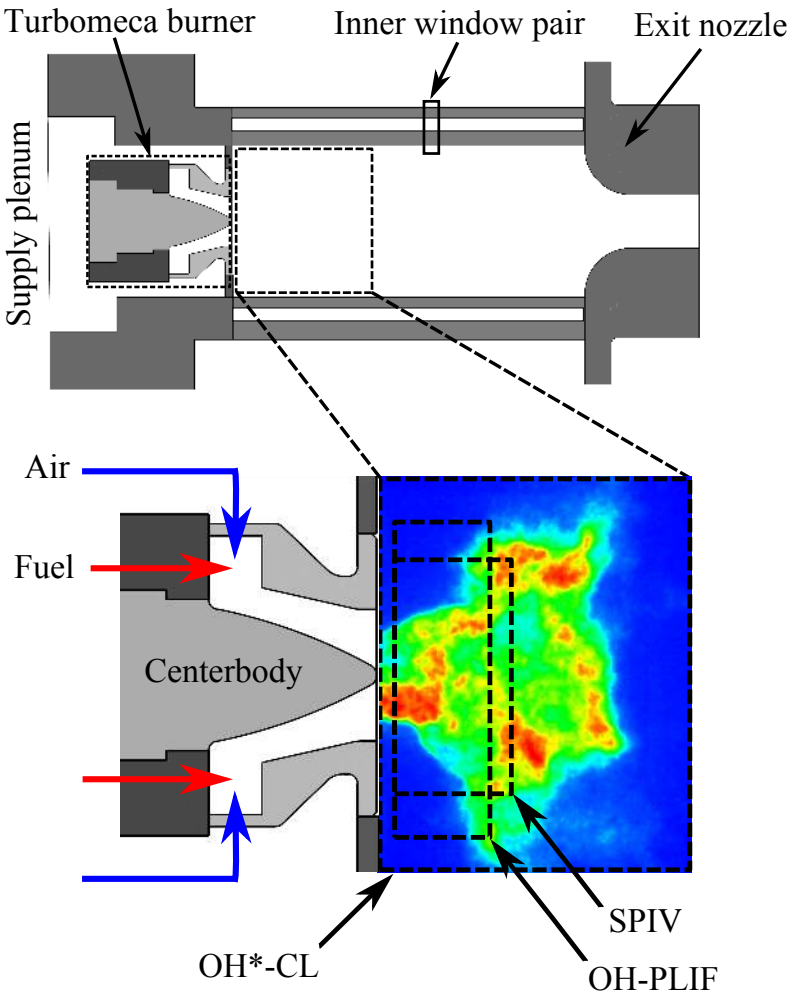

Figure 1: Schematic of Turbomeca (Preccinsta) burner installed into HIPOT test rig with measurement fields of view indicated.

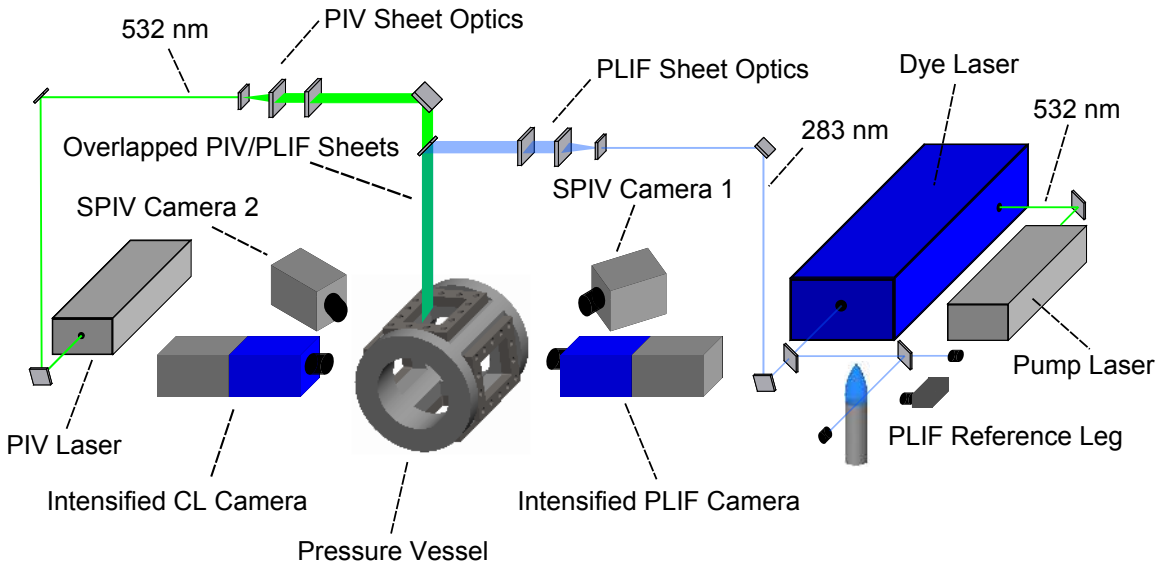

Figure 2: Schematic of measurement system.

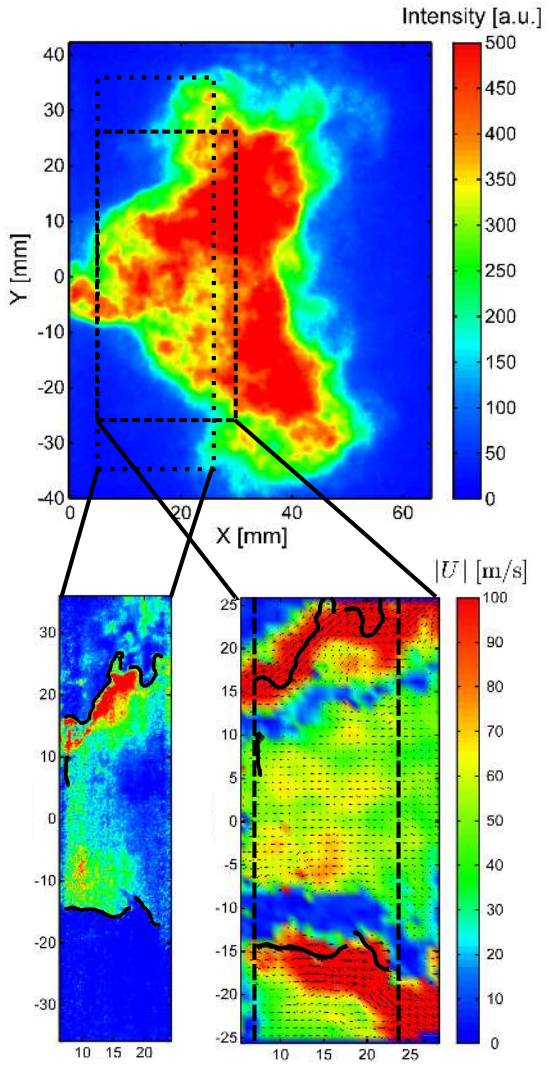

Figure 3: Typical instantaneous measurement fields simultaneously acquired under high-power flame conditions. The OH*-CL image (top) has the interrogation regions of the OH-PLIF (bottom, left) and SPIV (bottom, right) indicated. The dashed lines on the SPIV image indicate the overlapped region of the OH-PLIF field of view. The single-shot flame surface contour functions, extracted from the OH-PLIF signal gradient, are also overlaid against onto the OH-PLIF and SPIV data fields (thick black lines).

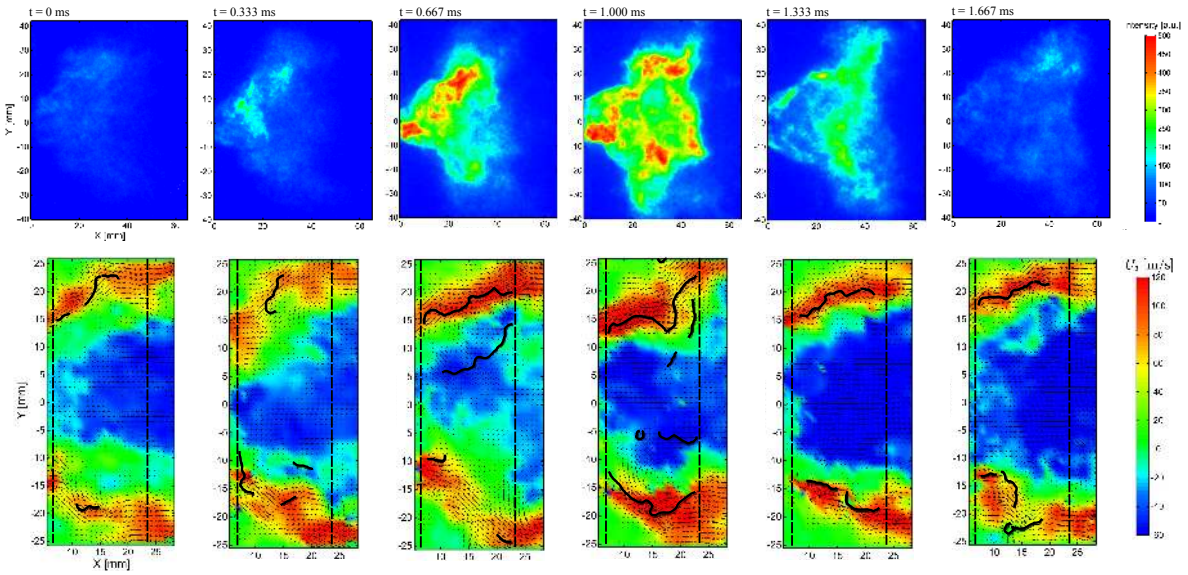

Figure 4: Typical measurement sequence acquired at a $3\,kHz$ interrogation frequency in the (unstable) flame B condition: OH*-CL intensity (top) and SPIV three-component vector fields overlaid against contours of axial velocity with flame surface contour functions plotted as solid black lines (bottom). The overlap region of the SPIV and OH-PLIF fields of view is indicated by dashed lines.

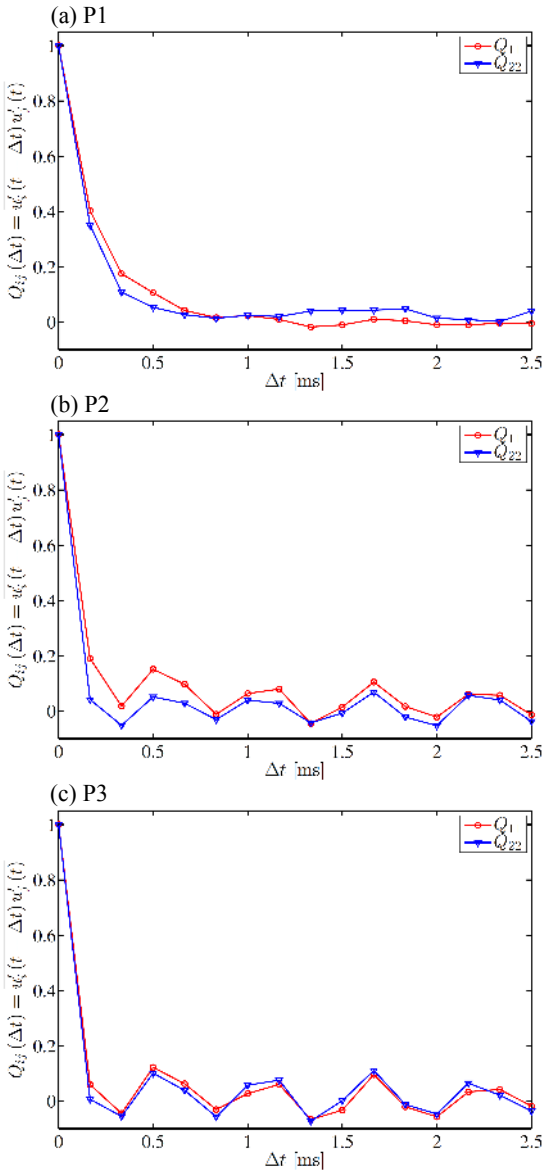

Figure 5: Time series autocorrelations of in-plane velocity components (U_x and U_y) at selected points in the nonreacting (NR) flow.

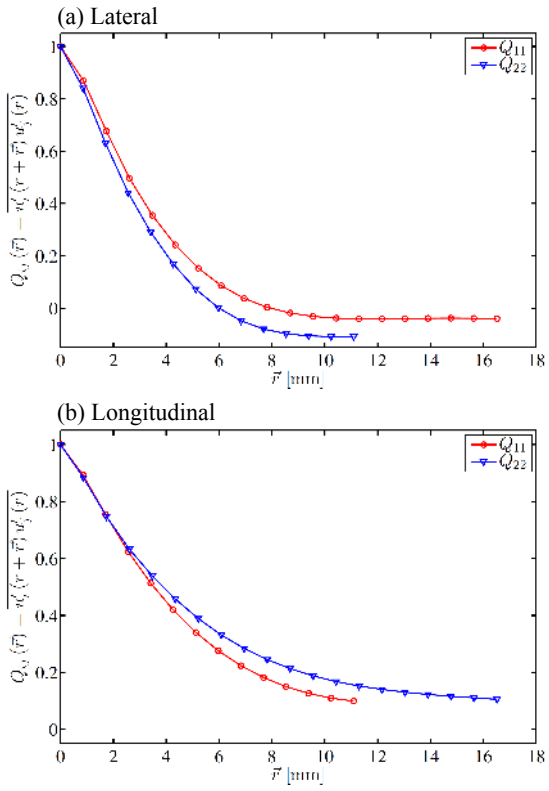

Figure 6: Lateral and longitudinal discrete spatial correlations of in-plane velocity components (U_x and U_y) in the nonreacting (NR) flow.

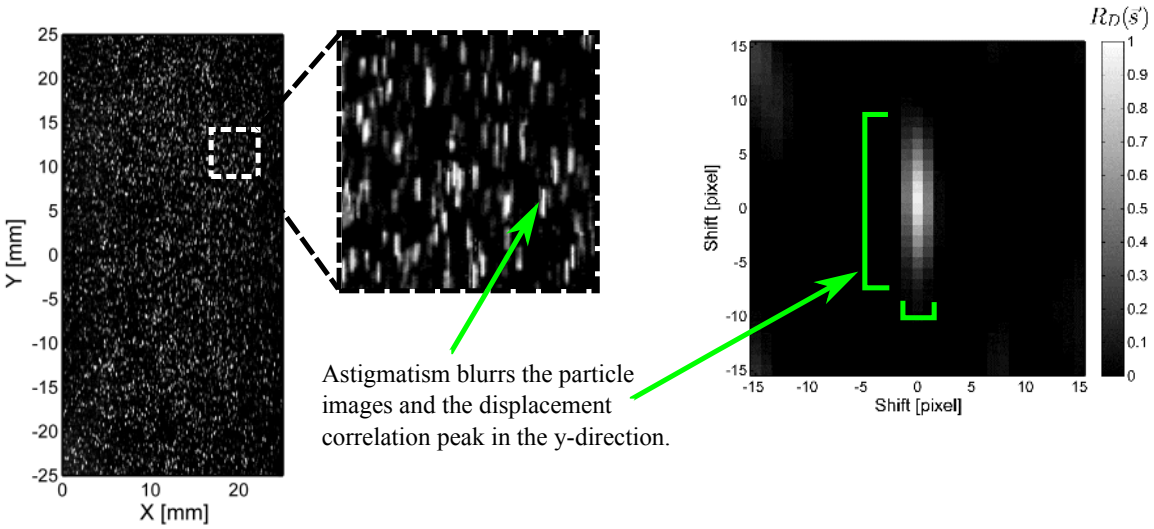

Figure 7: Astigmatism effects in the SPIV images as a result of the test rig windows.

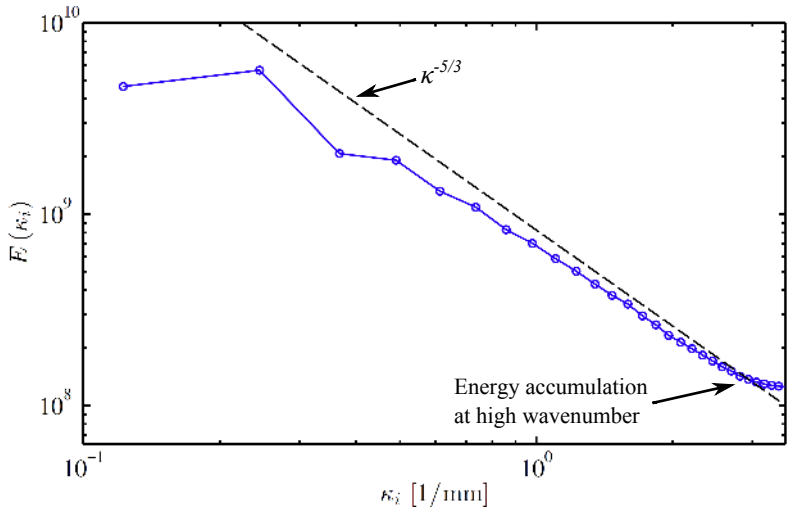

Figure 8: One-dimensional turbulent kinetic energy spectrum of the nonreacting (NR) flow.

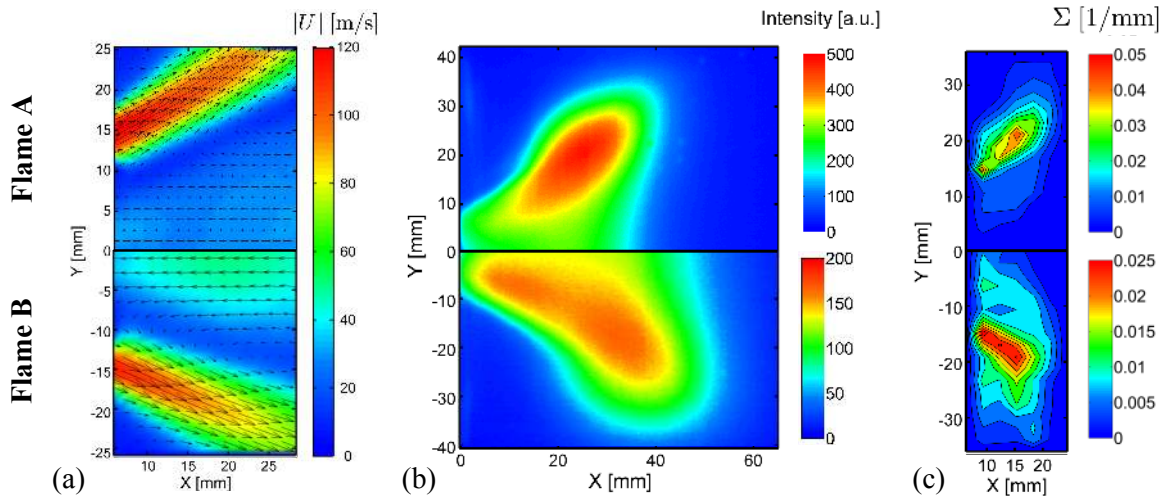

Figure 9: Time-averaged velocity field (a), OH*-CL emission (b), and flame surface density (c) measured in flame A (top) and flame B (bottom).

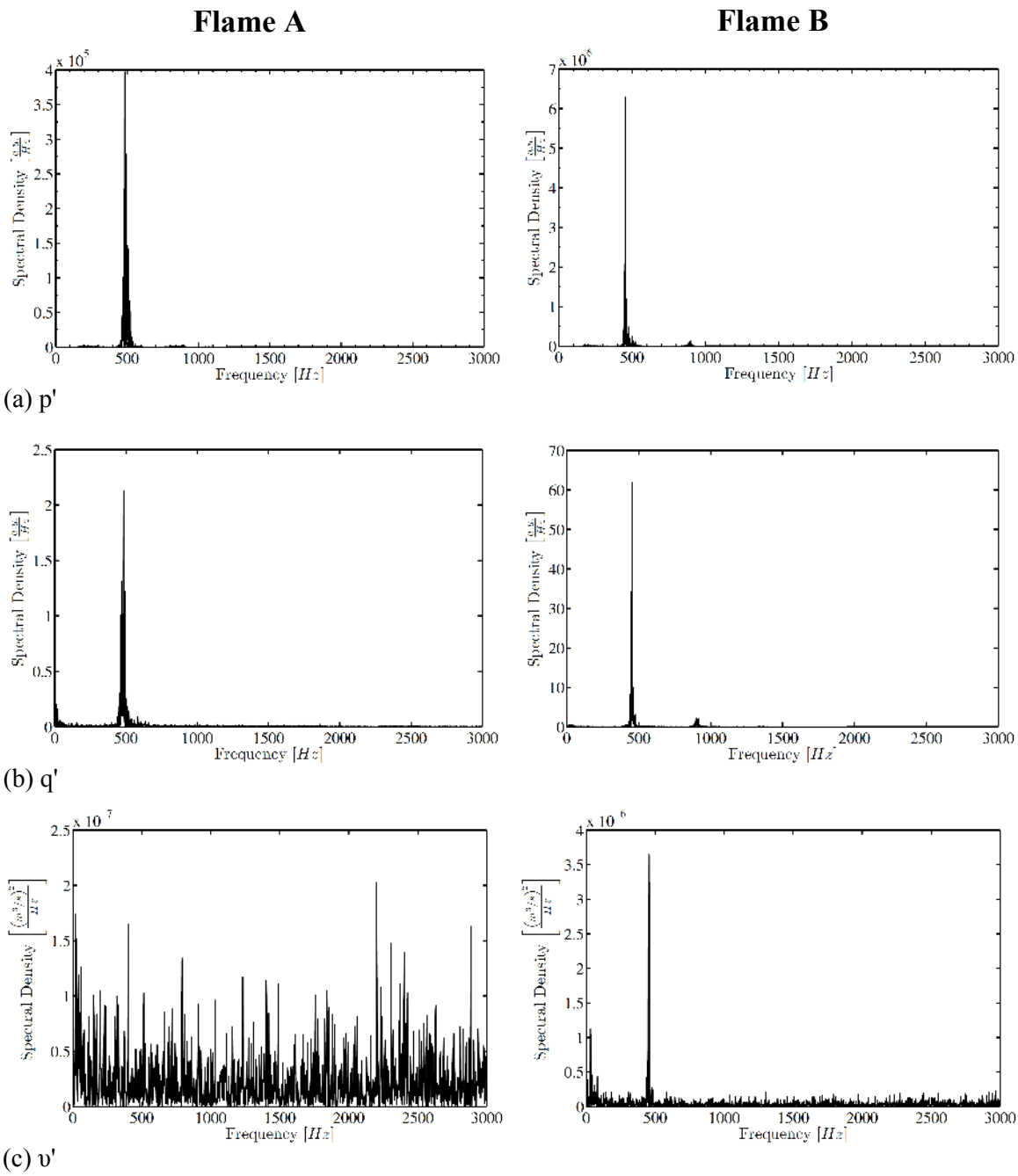

Figure 10: Power spectra of integrated signals.

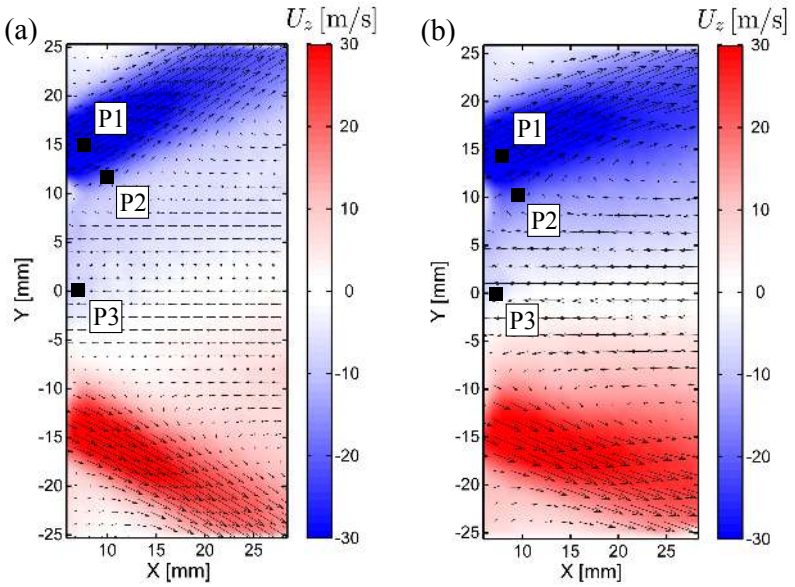

Figure 11: Probe locations represented in the time-averaged velocity fields.

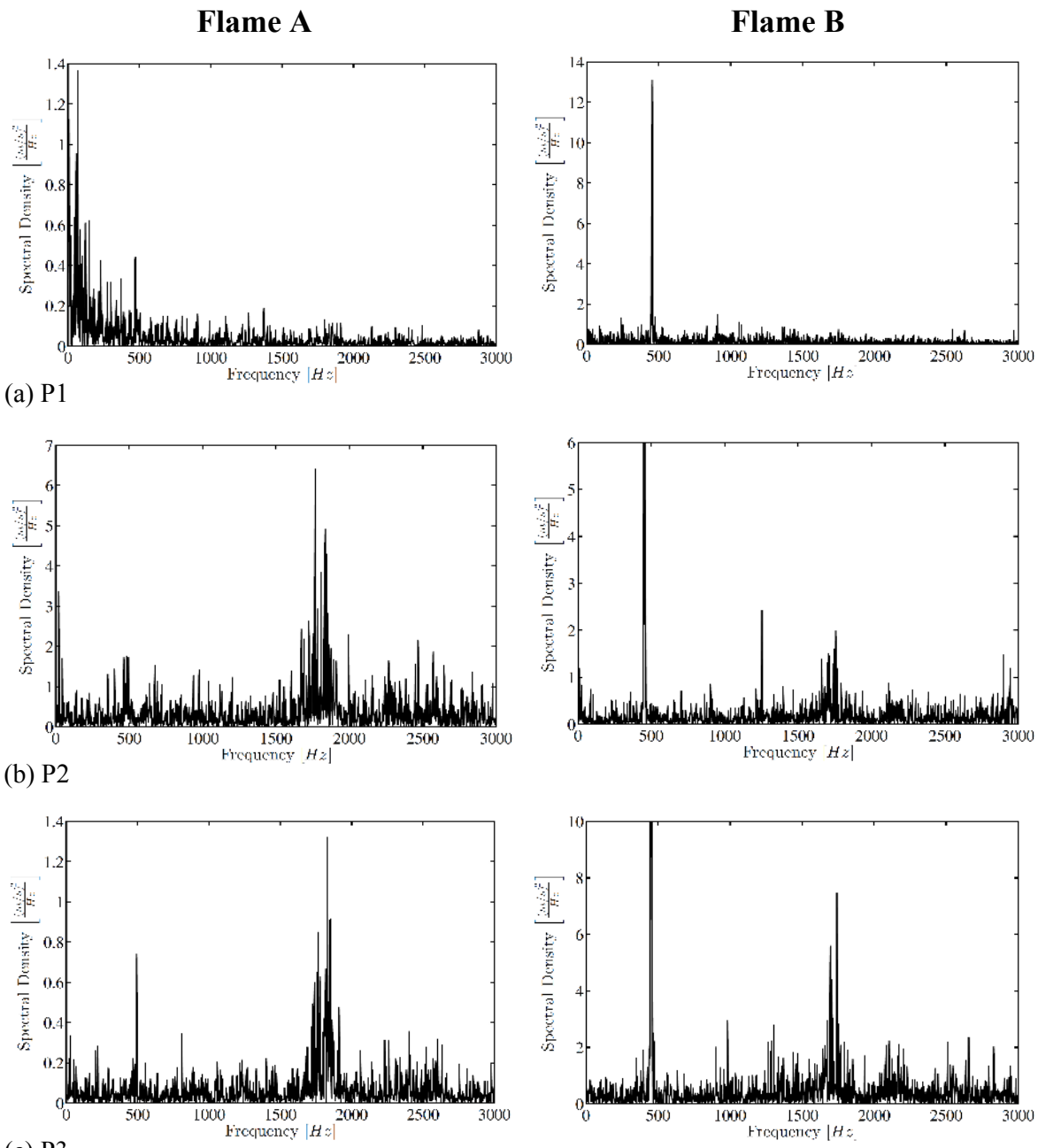

Figure 12: Power spectra of axial velocity at probe locations.

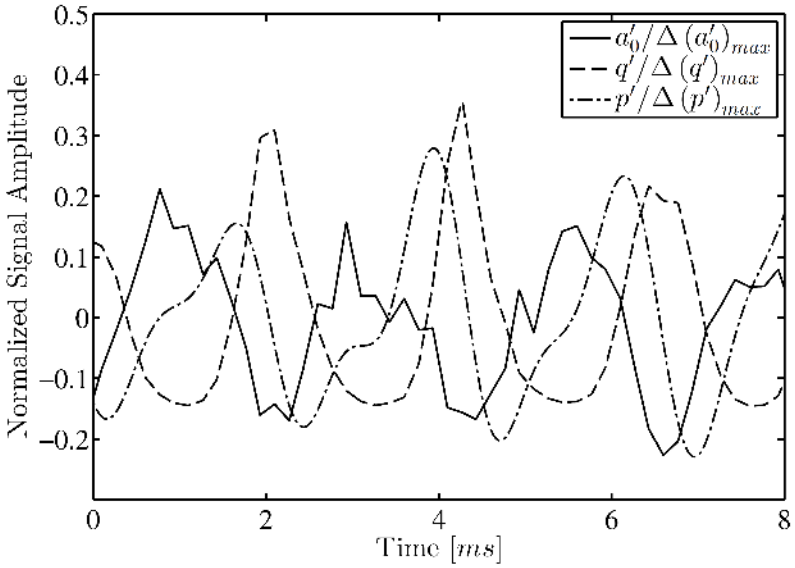

Figure 13: Time series of zeroth mode temporal coefficient plotted with integrated signals.

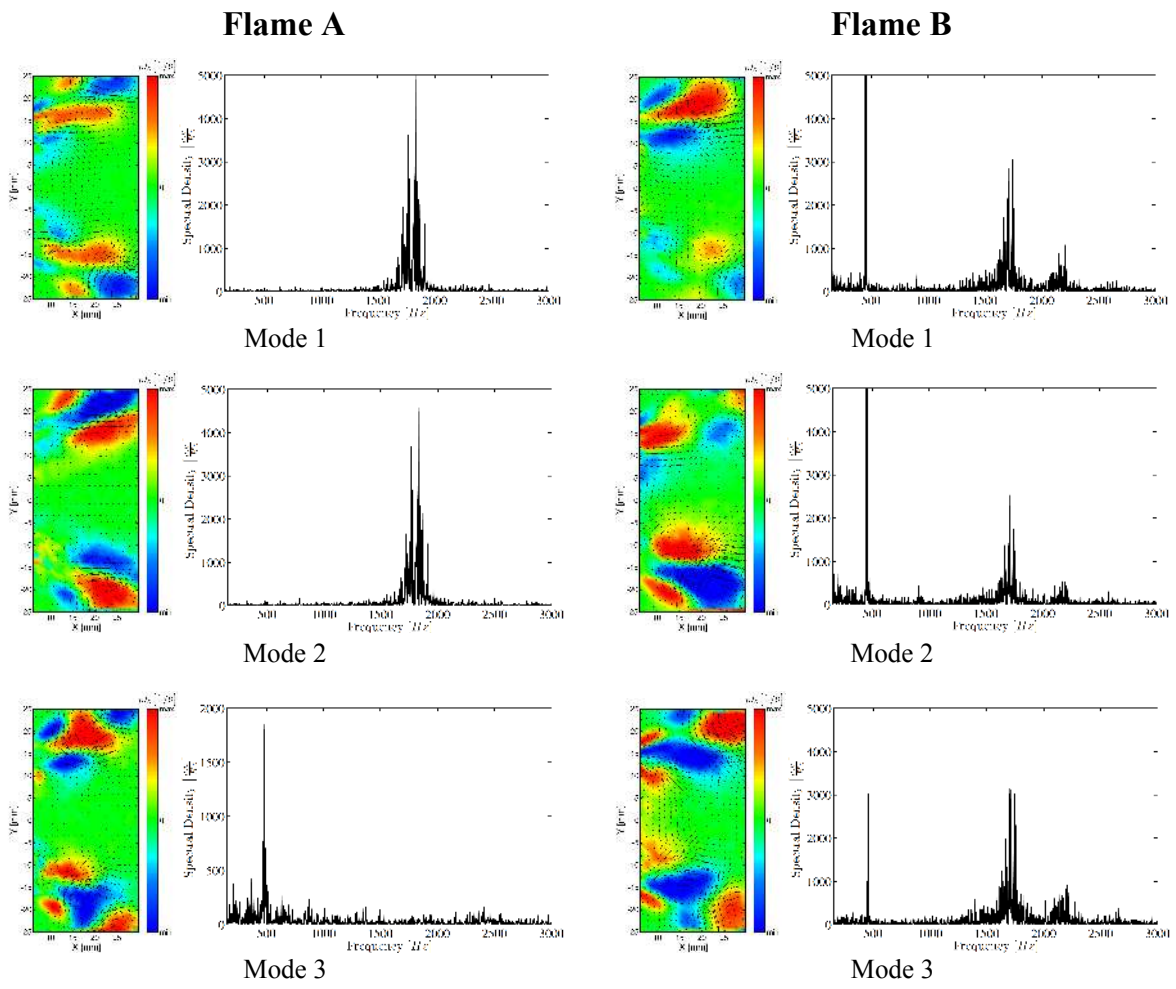

Figure 14: POD eigenmodes and power spectra of corresponding temporal coefficients.

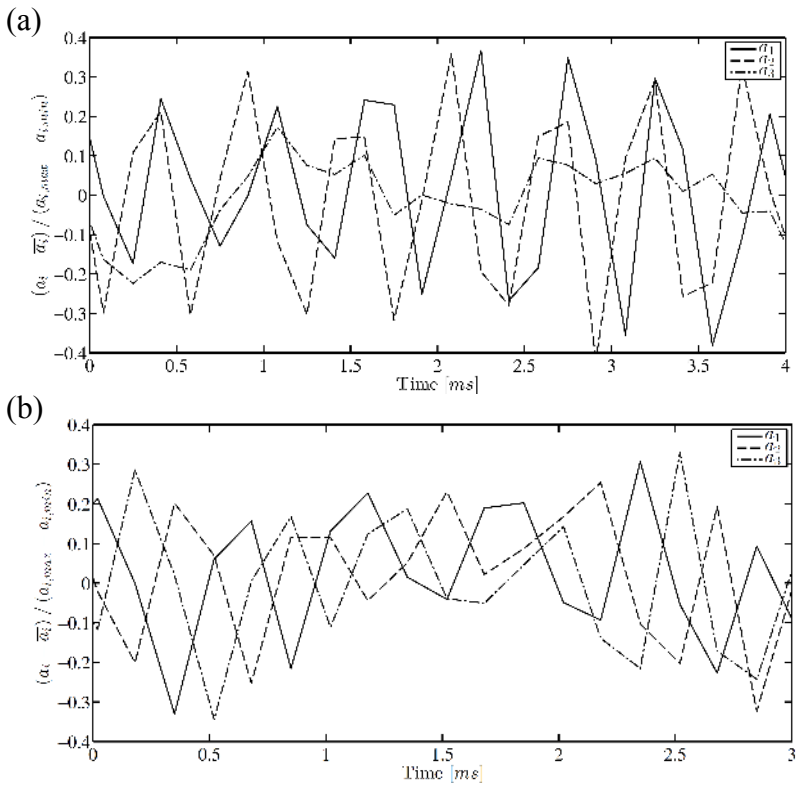

Figure 15: Time series of POD temporal coefficients from flame A (a) and flame B (b).

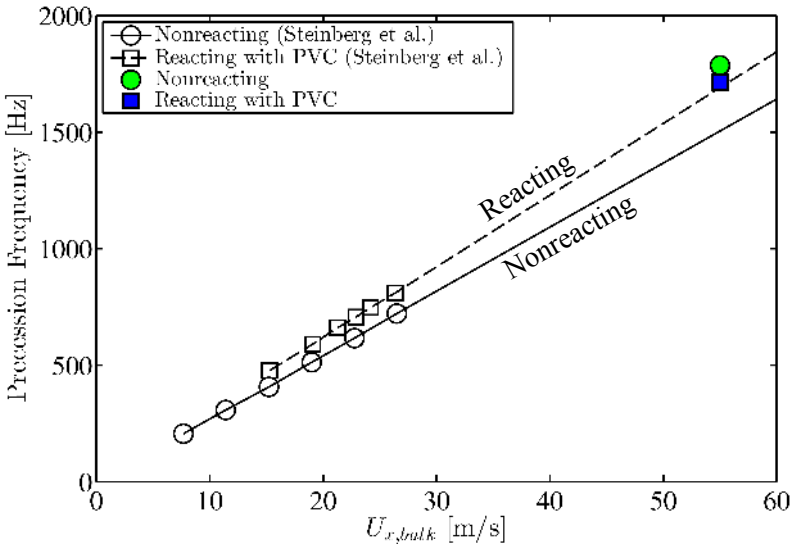

Figure 16: PVC precession frequency scaling.

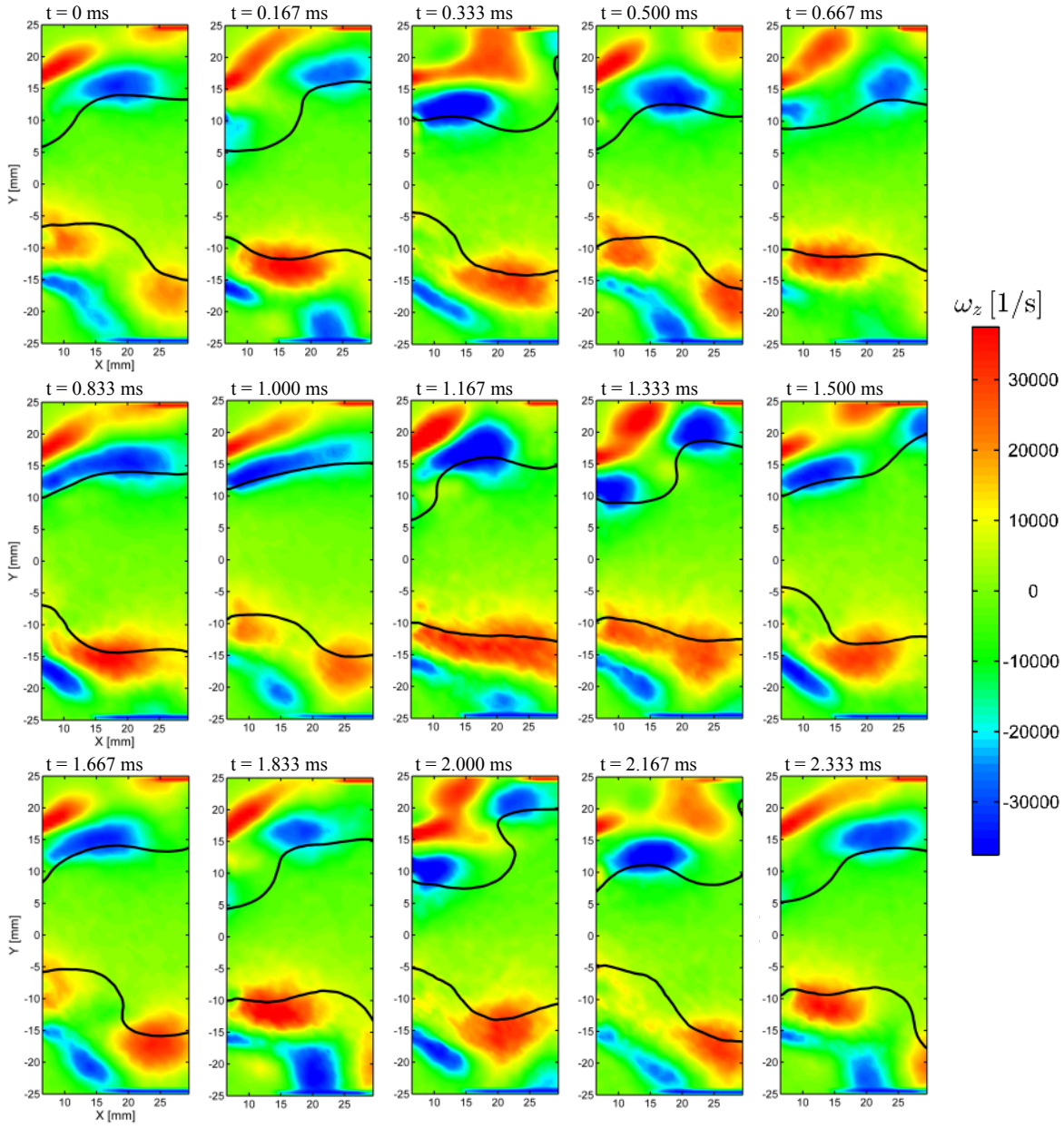

Figure 17: Sequence of reconstructed out-of-plane vorticity fields (ω_z) with central recirculation bubble boundary overlaid (indicated by solid black isocontour along stagnation line, $U_x = 0$).

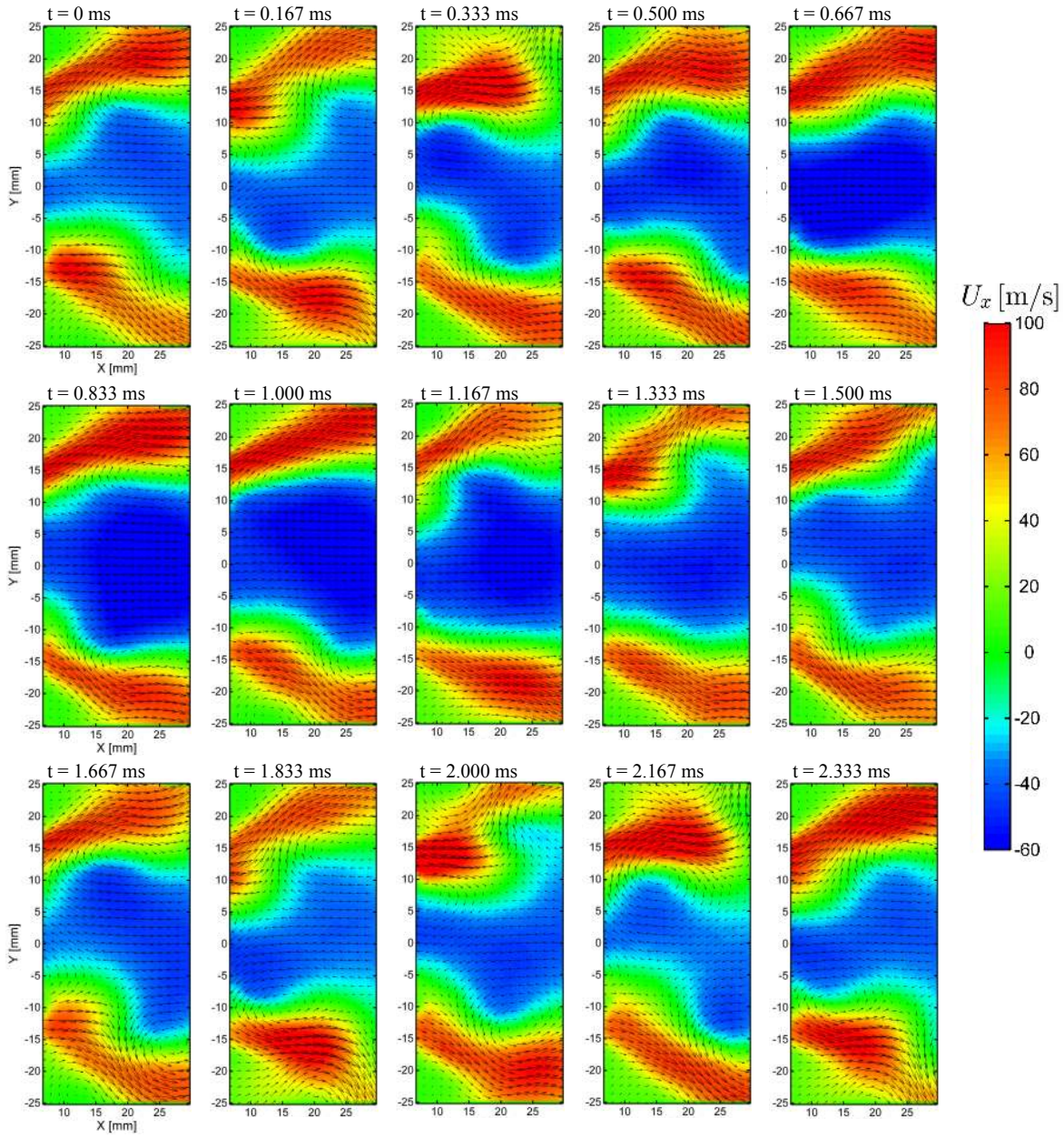

Figure 18: Sequence of reconstructed velocity fields plotted over contours of axial velocity (U_x).

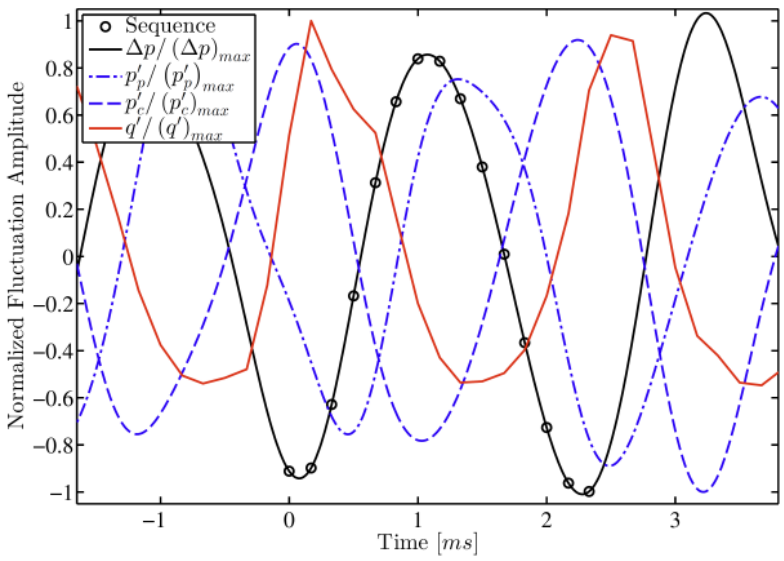

Figure 19: Time series of normalized injector pressure drop (Δp), chamber pressure fluctuation (p'), and heat release (q') with the optical data acquisition times indicated.

List of Tables

Table 1: Conditions studied.

Condition	Pressure [MPa]	Main Air Temperature [K]	$\dot{m}_{air}$ [g/s]	$\dot{m}_{fuel}$ [g/s]	ϕ	Power [kW]
A	0.5	600	88	3.6	0.70	180
B	0.5	600	88	3.3	0.58	150
NR	0.5	600	88	-	-	-